Ruddlesden-Popper-Phase Hybrid Halide Perovskite/Small-Molecule Organic Blend Memory Transistors

Murali Gedda, Emre Yengel, Hendrik Faber, Fabian Paulus, Joshua A Kress, Ming-Chun Tang, Siyuan Zhang, Christina A Hacker, Prashant Kumar, Dipti R Naphade, et al.

Ruddlesden-Popper Phase Hybrid Halide Perovskite/ Small-Molecule Organic Blend Memory Transistor

Murali Gedda*, Emre Yengel, Hendrik Faber, Fabian Paulus, Joshua A. Kreß, Ming-Chun Tang, Siyuan Zhang, Christina A. Hacker, Prashant Kumar, Dipti R. Naphade, Yana Vaynzof, George Volonakis, Feliciano Giustino, and *Thomas D. Anthopoulos**

Dr. M. Gedda, Dr. E. Yengel, Dr. H. Faber, Dr. M. C. Tang, Dr. P. Kumar, Dr. D. R. Naphade, Prof. T. D. Anthopoulos
King Abdullah University of Science and Technology (KAUST),
KAUST Solar Center (KSC),
Thuwal 23955-6900,
Saudi Arabia
E-mail: thomas.anthopoulos@kaust.edu.sa; murali.gedda@kaust.edu.sa

Dr. F. Paulus, Joshua A. Kreß, Prof. Y. Vaynzof
Integrated Center for Applied Physics and Photonic Materials,
Center for Advancing Electronics Dresden (CFAED),
Technical University of Dresden,
Nöthnitzer Straße 61, 01187 Dresden,
Germany

Dr. S. Zhang, Dr. C. A. Hacker
Physical Measurement Laboratory,
National Institute of Standards and Technology (NIST),
Gaithersburg, Maryland 20899, USA.

Dr. S. Zhang
Theiss Research, La Jolla, CA 92037, USA

Dr. G. Volonakis,
Univ Rennes, ENSCR, INSA Rennes, CNRS, ISCR (Institut des Sciences Chimiques de Rennes), UMR 6226, Rennes F-35000, France

Prof. F. Giustino
Oden Institute for Computational Engineering and Sciences, The University of Texas at Austin, Austin, Texas 78712, USA
Department of Physics, The University of Texas at Austin, Austin, Texas 78712, USA
.

Abstract

Controlling the morphology of metal halide perovskite layers during processing is critical for the reliable manufacturing of optoelectronic devices. Here we report on a strategy to control the microstructure of solution-processed layered Ruddlesden-Popper phase perovskite films based on $(PEA)_2PbBr_4$. The method relies on the addition of the organic semiconductor C_8-BTBT directly into the perovskite formulation, where it facilitates the formation of large and near-single-crystalline quality platelet-like $(PEA)_2PbBr_4$ domains overlaid by a ≈5-nm-thin C_8-BTBT layer. Transistors with $(PEA)_2PbBr_4/C_8$-BTBT channels exhibit unexpectedly large hysteresis window between forward and return bias sweeps. Material and device analysis combined with theoretical calculations suggest that the C_8-BTBT-rich phase acts as the hole transporting channel, while the quantum wells in $(PEA)_2PbBr_4$ beneath act as the charge storage element where carriers from the channel are injected, stored or extracted via tunnelling. When tested as a non-volatile memory, the devices exhibit record memory window (>180 V), a high erase/write channel current ratio (10^4), good data retention and high endurance (>10^4 cycles). Our results highlight a new memory device concept for application in large-area electronics while the simple growth technique adopted could potentially be exploited for the development of other optoelectronic devices including solar cells, photodetectors and light-emitting diodes.

Main Text

Organic metal halide Ruddlesden–Popper phase perovskites are currently attracting increasing attention due to their superior chemical stability and resistance against humidity which makes them attractive for use in emerging optoelectronic applications including, solar cells, light-emitting diodes, field-effect transistors, resistive switches and memristors, to name but a few.[1–3] To this end, different strategies have been explored to further improve the device performance and stability, including the synthesis of new materials, the use of innovative processing methodologies, and implementation of novel device architectures.[4,5] Among these strategies, morphology engineering of the active perovskite layer has emerged as a promising route towards enhancing the film crystallinity and performance of the resulting devices.[4–7]

Although in the field of photovoltaics the use of polycrystalline perovskite layers can still yield cells with high power conversion efficiency (PCE),[8] the situation is markedly

different in thin-film transistors (TFTs) where the presence of grain boundaries has a detrimental effect in lateral charge transport.[9–11] Thus for the development of reliable, high performance TFTs, the ability to simultaneously control the layer morphology and crystallinity becomes critical. In recent years, various approaches have been developed and implemented, including the use of additives, solvent and compositional engineering, thermal treatment, all the way to the incorporation of self-assembled monolayers (SAMs) for interface engineering.[4–7] Among the various approaches reported, blending with an insulating polymer (i.e. composition engineering) has shown promise for controlling the perovskite layer morphology, albeit with limited success in terms of device performance due to the insulating nature of the polymer.[12,13]

Motivated by these early studies but also from similar approaches exploited in the field of organic semiconductors,[14–17] we investigated the possibility of controlling the crystallization kinetics of a layered hybrid perovskite by mixing it with a semiconducting organic small-molecule. In particular, we blended the 2D Ruddlesden–Popper phase perovskite (2D-RPP) phenethylammonium lead bromide ($(PEA)_2PbBr_4$)[18] with the molecular organic semiconductor 2,7-dioctyl[1]benzothieno[3,2-b] benzothiophene (C_8-BTBT),[19] and spin-coated the formulations at room temperature to form the solid layers (see *Experimental*). There are several reasons for choosing C_8-BTBT including its high solubility, good environmental stability and record high hole mobility.[19–22] Moreover, films of C_8-BTBT are known to form highly crystalline layered structures[21] that resemble those found in 2D halide perovskites such as $(PEA)_2PbBr_4$.[18,23] To this end, $(PEA)_2PbBr_4$ is a prototypical 2D lead halide perovskite system which has been extensively studied in recent years because of its environmental stability and tendency to form natural stack of quantum wells.[24,25] A pronounced effect on the morphology evolution of the resulting layer was observed and an optimal $(PEA)_2PbBr_4$:C_8-BTBT composition identified. X-ray photoelectron spectroscopy (XPS) depth profiling reveals the C_8-BTBT phase-separates vertically forming an ultrathin layer atop crystalline platelet-like $(PEA)_2PbBr_4$ domains, in a process closely resembling the vertical phase separation

encountered in organic polymer/small-molecule blends.[14–17] Using the hybrid bilayers as the channel results in transistors with extremely large, robust and temperature-independent operating hysteresis. Device analysis combined with theoretical calculations highlight the synergistic effects of hole transport along the C_8-BTBT-rich channel and quantum mechanical tunnelling in and out the natural quantum well (QW) of the $(PEA)_2PbBr_4$ crystal beneath, as the origin of the hysteresis. These programmable device operating characteristics[26] are exploited to demonstrate robust non-volatile memory transistors that exhibit a large memory window (>180 V), high retention time (55,000 s), and high endurance (10,000 cycles) while maintaining a large current on/off ratio (10^4).

The $(PEA)_2PbBr_4$ and C_8-BTBT (**Figure 1a**) solutions were prepared separately and mixed at a later stage to form the various blend formulations (see *Experimental*). Three different perovskite/small-molecule volume ratios (vol%) were studies: 90/10 vol% (Blend-I), 75/25 vol% (Blend-II), and 50/50 vol% (Blend-III). All formulations were processed via spin-coating at room temperature inside a nitrogen-filled glovebox followed by thermal annealing (see *Experimental*). Polarized-light optical microscopy (POM) images of the formed layers are shown in **Figure S1** (*Supporting Information*). With the exception of Blend-II, all other layers appear heterogeneous and exhibit no electrical functionality, and will be discussed in detail later. Blend-II formulation undergoes a clear and abrupt change during deposition yielding layers composed of large platelet-like domains (**Figure S1c**). The topography of these layers and was further investigated using atomic force microscopy (AFM) and compared to the pristine $(PEA)_2PbBr_4$ layer (**Figure 1b-c**). The neat $(PEA)_2PbBr_4$ layer appears polycrystalline and rough with an average thickness of ≈320 nm as compared to ≈230 nm for the Blend-II layer (**Figure 1b-c** and **Figure S2**) with the latter appearing significantly more homogeneous featuring large, percolating, platelet-like domains 10-50 µm in size (**Figure 1c**). Analysis of the AFM height histograms in **Figure S2b** reveals a distinct bimodal distribution indicative of the existence of two plateaus, one at ≈112 nm (Plateau-1) and a second (Plateau-2) at ≈263 nm.

We further investigated the crystallinity of the formed layers using X-ray diffraction (XRD) measurements. **Figure 1d** shows the diffractograms for the neat $(PEA)_2PbBr_4$ and Blend-II layers, while **Figure S3** displays the diffractograms for all four samples. The evenly spaced sharp diffraction peaks of (002) to (00 10) confirms the formation of the 2D-RPP perovskite phase with a preferential out-of-plane orientation in all samples. Analysis of the diffractograms in **Figure 1d** and **Figure S3** shows that Blend-II layers exhibit enhanced diffraction intensities and reduced peak widths, highlighting the key role of C_8-BTBT in mediating the crystallization and growth of the $(PEA)_2PbBr_4$ domains without distorting the 2D-RPP phase. Analysis of the (002) peak using the Debye-Scherrer method[27] reveals a significant increase in the crystallite size from ≈75 nm, for neat $(PEA)_2PbBr_4$, to ≈123 nm for Blend-II layers (**Table S1**). The significant enlargement in the crystalline domains is expected to benefit carrier transport due to the presence of fewer grain boundaries.[28,29]

To probe the influence of C_8-BTBT on the perovskite orientation with respect to the substrate, we performed two-dimensional XRD (2D-XRD) measurements (**Figure 2a**). The resulting diffractograms for the neat C_8-BTBT films show a major reflection at 3.10° corresponding to (001) plane (see red dotted line in **Figure 2b**), in agreement with previous reports.[30] The neat $(PEA)_2PbBr_4$ layer, on the other hand, exhibits partial Debye-Scherrer diffraction rings with intense broad spots, which indicate the presence of mixed 2D-RPP phases corresponding to the different number of octahedron layers in the $(PEA)_2PbBr_4$ (i.e. different n number), with considerable randomness in their orientation with respect to the substrate (see schematic illustration in **Figure 2c**).[31] The central reflections at $\beta = 0°$ are attributed to the (002) planes of the 2D perovskite and the calculated layer spacing of ≈1.65 nm is in line with reports in the literature.[32,33] By contrast, Blend-II layers (**Figure 2a**) exhibit well-separated in-plane and out-of-plane diffraction spots, which are indicative of the presence of a single-crystalline phase with $n = 1$.[31] **Figure 2c-d** depicts the orientation of the domains in $(PEA)_2PbBr_4$ formed without and with C_8-BTBT, respectively, with respect to the substrate.

Calculating the full width at half maximum (FWHM) of the higher-order (002) reflections for the neat perovskite and Blend-II films, reveals that the latter exhibits consistently lower values, indicating the presence of larger crystalline domains as compared to neat $(PEA)_2PbBr_4$ (**Figure S4**). On the basis of these results we conclude that although the crystal lattice of $(PEA)_2PbBr_4$ remains unaffected by the presence of C_8-BTBT, the size, crystallinity and preferred orientation of the $(PEA)_2PbBr_4$ domains increases significantly.

Next, we studied the elemental composition and distribution in Blend-II layers using X-ray energy dispersive spectroscopy (EDS) (**Figure 3a**). The elemental maps for C, S, and Br indicate the homogeneous distribution of the elements within individual platelet-like islands. Although the same is valid for C and S outside the crystalline domains, this is not the case for Br as it is found primarily in regions corresponding to the crystalline platelet-like $(PEA)_2PbBr_4$ domains. We thus conclude that C_8-BTBT (C and S) is uniformly distributed across the entire layer, whereas $(PEA)_2PbBr_4$ (Br) is primarily confined to the platelet-like domains of the composite layer. Additional information about the elemental composition of Blend-II layers was obtained via XPS measurements. **Figure 3b** shows the XPS spectra in the 195−135 eV range covering the Br 3p (195−175 eV), S 2p (165−160 eV), Si 2s (160−150 eV), and Pb 4f (150−135 eV) core levels. The practical advantage of this representation is that information related to the various elements (i.e. Br, S, and Pb) are acquired in the same spectral window giving accurate relative intensity ratio between them at a specific probing depth, which can be easily compared without elaborate calculations. For reference, the XPS spectra of the Br 3d, the highest intensity peak for bromine, is shown in **Figure S5**. As seen in **Figure 3b**, the Pb 4f peaks are only observed in the neat $(PEA)_2PbBr_4$ and the Blend-II layers, whereas the S 2p signature appears only in C_8-BTBT and Blend-II layers confirming that the organic molecule and perovskite phase co-exist.

To probe the elemental composition in the vertical direction of Blend-II layers, we performed XPS depth profiling measurements using an Ar ion gun with ≈0.21 nm/s sputtering

rate. The latter value was calculated by considering the time taken (≈1080 s) to fully etch the 230 nm-thick blend layer. The bottom panel in **Figure 3b** shows the XPS spectra in the 195-135 eV spectral range after the initial three sputtering steps (up to 90 s). The S 2p peak disappears after the first 30 s of sputtering (≈5 nm), which implies that C_8-BTBT is only distributed on the surface of the Blend-II layer. To study the vertical phase separation further we analysed the elemental composition of the blend layer using XPS depth profiling technique (**Figure S6**). Indeed, the results show that a thin C_8-BTBT layer exists at the top of the blend film (**Figure S6a**, region 1). The thickness of the layer is approximately 4-5 nm (**Figure S6b**) and is likely the result of the lower surface energy of C_8-BTBT as compared to the perovskite, which drives the phase separation. Beneath the C_8-BTBT layer, the film is dominated by elements associated with $(PEA)_2PbBr_4$ (**Figure S6a**, region 2) until the ITO substrate is reached (**Figure 6a**, region 3). These results provide direct evidence for the presence of a vertically phase-separated $(PEA)_2PbBr_4$/C_8-BTBT system. **Figure 3c** shows a schematic illustration (not to scale) of the spontaneously formed bilayer system.

The charge transport characteristics in all three blend layers were evaluated in bottom-gate, top-contact (BG-TC) transistors and compared against those of neat $(PEA)_2PbBr_4$ TFTs (**Figure S7**). As already mentioned, transistors based on Blend-II (**Figure 4a**) are the only devices exhibiting *p*-channel behavior featuring prominent counter-clockwise hysteresis in the channel current (I_D) when sweeping the gate voltage (V_G) from positive (+100 V) to negative (-100 V) and back to positive potential. Despite the large hysteresis, Blend-II TFTs maintain a high channel current modulation of $>10^4$ with the operating characteristics remaining similar even after 100 repeated measuring cycles (**Figure 4b**), and when measured at different V_D (**Figure 4c**). Analysis of the forward sweep in **Figure 4a** yields a maximum hole mobility in saturation for these transistors on the order of 5×10^{-2} cm^2 V^{-1}s^{-1}. These results suggest that in Blend-II transistors, hole accumulation occurs within the phase-separated C_8-BTBT-rich domain atop the $(PEA)_2PbBr_4$ crystalline platelets. Altering the concentration of C_8-BTBT in

the blend formulation leads to the formation of polycrystalline layers (**Figure S1**) and to non-functioning transistors (Blend-I and III in **Figure S7**). We attribute this to the unfavourable crystallization dynamics of the layer during spin-coating and the absence of any distinct phase separation between the two components. For this reason, TFTs based on Blend-I and Blend-III were not considered any further here.

The origin of operating hysteresis in TFTs can be broadly attributed to three main processes: Dipole polarization (process-I), the presence of mobile ions (process-II), and charge trapping (process-III).[34] Dipole switching (process-I) is commonly observed in memory transistors utilizing ferroelectric gate dielectrics.[34] The process typically manifests as clockwise hysteresis (*p*-channel devices), which is clearly not the case here and as such it can be excluded (**Figure 4a-c**).[26] Process-II, on the other hand, is known to induce counter-clockwise hysteresis which is qualitative similar to that observed in **Figure 4a** and is frequently encountered in semiconductors containing mobile ions, including metal halide perovskites.[35–37] In devices where process-II dominates, the hysteresis often depends on both the scan rate (V/s) of V_G during measurements, due to the field-driven displacement of mobile ions, and the sample temperature (T), since at low temperatures mobile ions freeze out. To test these hypotheses, we recorded the transfer characteristics for Blend-II transistor at different V_G scan rates from 1 to 5 V/s (**Figure 4d**) and at temperatures in the range 5-300 K (**Figure 4e**). Evidently, no systematic dependence of hysteresis on either measurement parameter is observed. The only noticeable change is the small shift in the turn-on voltage (V_{ON}) in the forward scans with lowering T (58 V at 300 K and 34 V at 5 K), an effect most likely attributed to the dependence of V_{ON} on T, often observed in organic TFTs due to carrier trapping at the interface[38,39], although other processes cannot be excluded. On the basis of these results, we conclude that mobile ion migration cannot explain the hysteresis observed in $(PEA)_2PbBr_4/C_8$-BTBT transistors (**Figure 4a**). Charge trapping (process-III) is the only remaining process that could account for hysteretic behaviour observed. Indeed, the presence of trap states in the

channel of a *p*-type TFT is known to give rise to counter-clockwise hysteresis.[34] However, the latter is often accompanied by strong temperature dependence characteristics, which is not observed here (**Figure 4e**).

Next, we studied the influence of the applied gate field on the device hysteresis by recording the transfer curves at V_G sweeping ranges of ±25, ±30, ±50, ±75 and ±100 V at a constant V_D = -10 V (**Figure 4f**). What becomes evident from these measurements is that a minimum V_G bias of ±25 V is required for I_D to reach its maximum/minimum values (ON/OFF currents, respectively), suggesting that the gate field plays a key role in the hysteresis. Such a robust, temperature-independent and vertical electric-field dependent channel conductance behavior points to the presence of a "floating-gate" like system where charge trapping/de-trapping occurs via quantum mechanical tunnelling - a largely temperature-independent process.[40–42] By considering the phase-separated channel depicted in **Figure 5a**, we hypothesize that the natural QW formed within the $(PEA)_2PbBr_4$ platelet-like crystals beneath the C_8-BTBT phase may act as the floating-gate able to capture holes upon application of an electric field during the device operation. Under charge accumulation conditions (ON state), holes injected in the conjugated BTBT core start to tunnel across the insulating C_8/PEA spacers (≈1.3 nm distance) to the $PbBr_4$ QW beneath via electric-field-assisted tunnelling (**Figure 5b**) in a process described previously for layered hybrid perovskites.[25] The ability of the layered hybrid perovskites, such as $(PEA)_2PbBr_4$, to suppresses ion-migration[43] may also explain the absence of ionic displacement in the temperature dependent measurements shown in **Figure 4e**. This is a key observation that supports the aforementioned tunnelling-mediated trapping/detrapping process proposed.

In an effort to quantitatively describe the energy level alignment between C_8-BTBT and $(PEA)_2PbBr_4$, which is needed to support the quantum confinement and tunneling effects, we employed density functional theory (DFT) based calculations, using the Heyd–Scuseria–Ernzerhof (HSE) hybrid functional (see *Supporting Information*).[44] **Figure S8a** shows the

calculated energy level alignment of $(PEA)_2PbBr_4$ and the molecular crystal of C_8-BTBT based on the density-of-states calculations shown in **Figure S8b**. The energy levels of the two systems are aligned with respect to each other, using the measured valence band top of -6.30 eV[45] and -5.05 eV[46] for $(PEA)_2PbBr_4$ and C_8-BTBT, respectively. The resulting energy band diagram (**Figure S8a**) corresponds to a type-II band alignment between $PbBr_4$ and BTBT, and type-I between PEA and $PbBr_4$ that forms the QW where PEA is the barrier layer. This is not surprising since 2D-perovskites are known to act as naturally occurring QW systems.[24,25] Based on the calculated density of states, C_8-BTBT can be also considered as a QW with the C_8 alkyl side chain confining the semiconducting back-bone (**Figure S8b**). The calculated lengths of the confinement layers are 10 and 16 Å for $(PEA)_2PbBr_4$ and C_8-BTBT, respectively. Overall, both energy band alignment and length of confinement support the injection/extraction of carriers in the perovskite QW through quantum mechanical tunnelling across the organic spacers (potential barriers) form the C_8-BTBT channel, and at the same time explain the temperature-independent hysteresis observed (**Figure 4e**).

Having demonstrated the ability to reliably modulate the conductance state of the $(PEA)_2PbBr_4/C_8$-BTBT channel via the V_G field, we explored the use of Blend-II transistor as a non-volatile memory device. **Figure 5c** shows the transfer characteristic of a representative device and the V_G bias chosen to write, read and erase the conductance state of the channel, which represents the bit of data stored, i.e., ON state, and OFF state. **Figure S9a** shows the device energy band diagram, reconstructed using the calculated energetics from **Figure S8b**, while **Figure S9b-d** depicts the energy diagram at different biasing conditions [i.e., $V_G = 0$ V (read), forward sweep V_G, (write) and return sweep V_G (erase)]. As already discussed, the key to the hysteretic behavior of these devices is the polarity and magnitude of V_G since it determines the probability of carrier tunnelling from BTBT to the $PbBr_4$ QW across the ≈1.3 nm-thick organic spacers (**Figure 5b**). The presence, or absence, of holes into the QW affects

the electrostatic potential landscape across the channel, ultimately determining the channel conductivity.

As shown in **Figure S9b**, prior to any V_G application, the octahedral PbBr$_4$ floating gate (i.e., the natural QW) is assumed neutral (no trapped charge). When the V_G becomes more negative with respect to the ground potential (source) (**Figure S9c**), holes start to accumulate in the BTBT phase while simultaneously being injected into the PbBr$_4$ QW via tunneling.[47] Under this biasing condition, the channel current reaches a maximum value of $\approx 10^{-5}$ A (ON-current) at $V_G = -100$ V (**Figure 5c**). Removing the V_G bias results in holes being confined inside the QW, unable to escape due to the presence of the insulating barrier layers on either side (**Figure 4b**, **Figure S8b**). The bit of data stored can then be readout by measuring the device current at $V_G = 0$ V ("read" potential in **Figure 5c**). When a less negative V_G is applied (**Figure S9d**), the concentration of holes in the C$_8$-BTBT channel quickly diminishes, while holes confined in the PbBr$_4$ QW are simultaneously pumped back (i.e. de-trapped) to the C$_8$-BTBT channel via the same tunnelling process. As the holes become fully depleted, the channel current reaches its lowest value of $\approx 3 \times 10^{-9}$ A (OFF-current) (**Figure 5c**) and it remains low until biasing with a more positive voltage (+100 V).

The large hysteresis window (ΔV_M) that envelopes the two conduction states remains unchanged during repeated measurements and exceeds 180 V (**Figure S10a**). The change of turn-off voltage (ΔV_{OFF}) measured during the return sweeps and ON/OFF ratio of the device during the 100 consecutive measurements (**Figure S10b**). The latter value is higher than any ΔV_M reported previously for organic TFT-based memory device. However, we note that considering the magnitude of ΔV_M alone without taking into account the V_G range employed, would be misleading. In an effort to objectively compare our data with results from the literature, we calculated the ratio of ΔV_M with the operating voltage range (V_{OP}) applied at the gate terminal (i.e., $\Delta V_M/V_{OP}$). The calculated values, together with those extracted from the literature,

are summarized in **Table S2**. Evidently, the $(PEA)_2PbBr_4/C_8$-BTBT transistors yield a $\Delta V_M/V_{OP}$ of ≈0.9, which is the highest reported value to date for organic TFTs.[48–57]

To evaluate the suitability of Blend-II transistors as a practical non-volatile memory device, we studied the endurance and data retention characteristics at room temperature. **Figure 5d** displays the endurance results for a device subjected to 10,000 repeated programming cycles (write, read and erase steps) using the gate voltage waveform shown in the inset. The channel current in both ON and OFF states remain almost unaltered, highlighting a robust device operation. Next, we investigated the ability of Blend-II transistors to retain the programmed data as a function of time; the so-called data retention time. For the purpose of this experiment, a single writing (or erasing) voltage pulse was applied to the gate terminal, followed by sequential reading steps at predefined time intervals over a period of 55,000 s. **Figure 5e** illustrates the evolution of both the ON and OFF currents across the device as a function of time following the application of the programming step i.e., write or erase (see inset in **Figure 5e**). Evidently, the device is able to retain the pre-programmed ON or OFF state over the entire testing period, suggesting a much longer intrinsic data retention time. Lastly, we evaluate the memory performance as a function of programming (writing/erasing) speed. As shown in **Figure 5f**, even the shortest pulse of 200 ms is sufficient to program the ON and OFF states in the device, with only a small decrease observed in the ON current for the shortest pulse width. Although scaling-down the channel length is anticipated to lead to faster programming times, the achieved speed is already adequate for a variety of low-end applications and is comparable with previously reported values for organic-based memories TFTs (**Table S2**).

To summarize, we have reported on a new strategy to grow crystalline hybrid perovskite/small-molecule bilayers via one-step solution processing. The organic molecule was shown to play a key role in controlling the crystallization and growth of the 2D-RPP perovskite phase, leading to the spontaneous formation of platelet like domains with near single-crystalline quality overlaid by a thin small-molecule layer. Transistors made with the hybrid bilayer as the

channel exhibited surprisingly large operating hysteresis, a property related to synergistic hole transport across the small-molecule phase atop and the simultaneous field-drivel carrier de/trapping from the natural quantum well in the perovskite beneath. When tested as non-volatile memory device, the transistor showed a large memory window of 180 V with a ΔV_M /V_{OP} ratio of 0.9; the highest reported to date for organic TFT memory devices (**Table S2**). The exceptional endurance demonstrated combined with promising data retention and the high current ON/OFF ratio achieved, makes the proposed memory transistor concept promising for application in large-area electronics. Lastly, we anticipate our approach to control the microstructure of hybrid perovskites may find use in different device applications including light-emitting diodes, solar cells and photodetectors, to name but a few.

Experimental

Material Preparation: The $(PEA)_2PbBr_4$ precursor solution of 0.2 M concentration was prepared by dissolving 1:2 molar ratio of $PbBr_2$ and $C_6H_5C_2H_4NH_3Br$ (PEABr) in dimethylformamide (DMF) while heated at 75 °C and under dynamic mixing for 5 h. The C_8-BTBT solution of 0.02 M was prepared separately using chlorobenzene (CB) as the solvent. The blend precursor formulations were prepared with three different perovskite/organic volume ratios (vol%) of: 90/10 (Blend-I), 75/25 (Blend-II) and 50/50 (Blend-III). The resulting precursor solutions appeared clear with no evidence of precipitation even after two weeks of storage at room temperature inside a nitrogen glovebox.

Transistor fabrication and characterization: The transistors in a back gate – top contact (BG-TC) architecture were fabricated on heavily doped Si (Si^{++}) wafers with 300 nm thermally grown SiO_2, acting as the gate electrode and gate dielectric, respectively. Before thin-film deposition, the Si^{++}/SiO_2 wafers were thoroughly cleaned using a series of ultra-sonication baths of de-ionized (DI) water, acetone and 2-propanol for 10 min each, followed by a UV-ozone

treatment step for 15 min. The pre-prepared formulations were spun on Si^{++}/SiO_2 substrates at 2000 rpm for 30 s followed by thermal annealing at 70 °C for 5 min in a dry nitrogen atmosphere. Transistor fabrication was completed by the thermal deposition of a top Au source and drain electrodes under a high vacuum (~1×10^{-6} mbar). The channel width (W) and length (L) of the resulting devices were 1000 µm and 40 µm, respectively. The electrical current-voltage characterization of the transistors at room temperature was carried out in a nitrogen glove box using a precision source/measure unit, B2912A (Keysight Technologies). A home-built MATLAB script has been employed to probe various characteristics of a memristor.

X-ray Diffraction Measurements: Bruker D8 ADVANCE diffractometer with a monochromatic Cu - K_α radiation beam with wavelength $\lambda = 0.154$ nm was used for X-ray diffraction measurements. The thin-films were studied in powder diffraction mode using θ–2θ scan configuration to detect crystallites with a reciprocal lattice vector perpendicular to the film surface.

Atomic Force Microscopy: The surface topography information for all the samples was measured via intermittent contact mode AFM using a ND-MDT SOLVAR NEXT scanning probe microscope in the air at room temperature. The measurements were performed using Pt/Ir coated Si tips of resonance frequency ranging between 150-300 Hz.

SEM imaging and EDX Mapping: Zeiss MERLIN Field Emission Scanning Electron Microscope (FESEM) with OXFORD EDS was used to characterize the surface morphology of obtained material and elemental mapping. X-ray energy of 25 kV was maintained while scanning the samples.

2D X-ray Diffraction: The XRD measurements of the organic, perovskite and blend films were conducted on a Rigaku SmartLab diffractometer equipped with a 9 kW rotating copper anode. The 2D diffraction maps were recorded using a 2D HyPix3000 detector in a coupled θ − 2θ

scan (beam collimator 0.2 mm φ) at a detector distance of 110 mm. The direct beam was

blanked with a beam blanker. Data processing, optics and sample alignment, and measurements

were performed using the Rigaku SmartLab Guidance and 2DP software. The maps were

background corrected. 1D profiles were obtained by integrating a central slice of the corrected

2D map, representing a standard Bragg-Brentano scan. Intensities (log scale) were normalized

to account for variations in film thickness and contributions from the k_β line were stripped.

XPS Depth Profiling: Kratos Axis UltraDLD XPS/UPS system, using the monochromatic Al

k_α line, is used to acquire XPS spectra. The base pressure of the analysis chamber is 10^{-8} Torr.

The spectra were calibrated with the C-C bond in C 1s peak, and set to BE = 284.5 eV. All

samples were characterized at a normal take-off angle unless stated otherwise. The Fermi level

was calibrated using atomically clean gold and the presented spectra were calibrated versus the

Fermi level at zero binding energy. XPS depth profiling is done by using an Ar-ion gun with

power 1 kV and 600 nA on a raster area of 1 mm^2.

Supporting Information
Supporting Information is available from the Wiley Online Library or from the author.

References

[1]   Z. Chen, Y. Guo, E. Wertz, J. Shi, *Adv. Mater.* **2019**, *31*, 1803514.

[2]   J. Hu, L. Yan, W. You, *Adv. Mater.* **2018**, *30*, 1802041.

[3]   Y. Lin, P. Pattanasattayavong, T. D. Anthopoulos, *Adv. Mater.* **2017**, *29*, 1702838.

[4]   C.-Y. Chang, C.-Y. Chu, Y.-C. Huang, C.-W. Huang, S.-Y. Chang, C.-A. Chen, C.-Y. Chao, W.-F. Su, *ACS Appl. Mater. Interfaces* **2015**, *7*, 4955.

[5]   Y. Li, L. Ji, R. Liu, C. Zhang, C. H. Mak, X. Zou, H.-H. H. Shen, S.-Y. Y. Leu, H.-Y. Y. Hsu, *J. Mater. Chem. A* **2018**, *6*, 12842.

[6]   P. Cheng, Z. Xu, J. Li, Y. Liu, Y. Fan, L. Yu, D.-M. Smilgies, C. Müller, K. Zhao, S. F. Liu, *ACS Energy Lett.* **2018**, *3*, 1975.

[7]   X. Zhang, R. Munir, Z. Xu, Y. Liu, H. Tsai, W. Nie, J. Li, T. Niu, D.-M. Smilgies, M. G. Kanatzidis, A. D. Mohite, K. Zhao, A. Amassian, S. F. Liu, *Adv. Mater.* **2018**, *30*, 1707166.

[8]   L. Gao, G. Yang, *Sol. RRL* **2019**, *4*, 1900200.

[9]   J. Qiu, Y. Zheng, Y. Xia, L. Chao, Y. Chen, W. Huang, *Adv. Funct. Mater.* **2019**, *29*, 1806831.

[10]   P. K. Nayak, D. T. Moore, B. Wenger, S. Nayak, A. A. Haghighirad, A. Fineberg, N. K. Noel, O. G. Reid, G. Rumbles, P. Kukura, K. A. Vincent, H. J. Snaith, *Nat. Commun.* **2016**, *7*, 13303.

[11]   J. G. Labram, D. H. Fabini, E. E. Perry, A. J. Lehner, H. Wang, A. M. Glaudell, G. Wu, H. Evans, D. Buck, R. Cotta, L. Echegoyen, F. Wudl, R. Seshadri, M. L. Chabinyc, *J. Phys. Chem. Lett.* **2015**, *6*, 3565.

[12]   T. H. Han, J. W. Lee, C. Choi, S. Tan, C. Lee, Y. Zhao, Z. Dai, N. De Marco, S. J. Lee, S. H. Bae, Y. Yuan, H. M. Lee, Y. Huang, Y. Yang, *Nat. Commun.* **2019**, *10*, 1.

[13]   A. Fakharuddin, M. Seybold, A. Agresti, S. Pescetelli, F. Matteocci, M. I. Haider, S. T. Birkhold, H. Hu, R. Giridharagopal, M. Sultan, I. Mora-Seró, A. Di Carlo, L. Schmidt-Mende, *ACS Appl. Mater. Interfaces* **2018**, *10*, 42542.

[14]   R. Hamilton, J. Smith, S. Ogier, M. Heeney, J. E. Anthony, I. McCulloch, J. Veres, D. D. C. Bradley, T. D. Anthopoulos, *Adv. Mater.* **2009**, *21*, 1166.

[15] A. F. Paterson, L. Tsetseris, R. Li, A. Basu, H. Faber, A. H. Emwas, J. Panidi, Z. Fei, M. R. Niazi, D. H. Anjum, M. Heeney, T. D. Anthopoulos, *Adv. Mater.* **2019**, *31*, 1900871.

[16] K. Zhao, O. Wodo, D. Ren, H. U. Khan, M. R. Niazi, H. Hu, M. Abdelsamie, R. Li, E. Q. Li, L. Yu, B. Yan, M. M. Payne, J. Smith, J. E. Anthony, T. D. Anthopoulos, S. T. Thoroddsen, B. Ganapathysubramanian, A. Amassian, *Adv. Funct. Mater.* **2016**, *26*, 1737.

[17] J. Panidi, A. F. Paterson, D. Khim, Z. Fei, Y. Han, L. Tsetseris, G. Vourlias, P. A. Patsalas, M. Heeney, T. D. Anthopoulos, *Adv. Sci.* **2018**, *5*, 1700290.

[18] K. Z. Du, Q. Tu, X. Zhang, Q. Han, J. Liu, S. Zauscher, D. B. Mitzi, *Inorg. Chem.* **2017**, *56*, 9291.

[19] H. Ebata, T. Izawa, E. Miyazaki, K. Takimiya, M. Ikeda, H. Kuwabara, T. Yui, *J. Am. Chem. Soc.* **2007**, *129*, 15732.

[20] K. Haase, C. Teixeira da Rocha, C. Hauenstein, Y. Zheng, M. Hambsch, S. C. B. Mannsfeld, *Adv. Electron. Mater.* **2018**, *4*, 1800076.

[21] R. Janneck, N. Pilet, S. P. Bommanaboyena, B. Watts, P. Heremans, J. Genoe, C. Rolin, *Adv. Mater.* **2017**, *29*, 1703864.

[22] A. F. Paterson, Y.-H. Lin, A. D. Mottram, Z. Fei, M. R. Niazi, A. R. Kirmani, A. Amassian, O. Solomeshch, N. Tessler, M. Heeney, T. D. Anthopoulos, *Adv. Electron. Mater.* **2018**, *4*, 1700464.

[23] F. Zhang, H. Lu, J. Tong, J. J. Berry, M. C. Beard, K. Zhu, *Energy Environ. Sci.* **2020**, *13*, 1154.

[24] M. Kepenekian, B. Traore, J. C. Blancon, L. Pedesseau, H. Tsai, W. Nie, C. C. Stoumpos, M. G. Kanatzidis, J. Even, A. D. Mohite, S. Tretiak, C. Katan, *Nano Lett.* **2018**, *18*, 5603.

[25] B. Traore, L. Pedesseau, L. Assam, X. Che, J. C. Blancon, H. Tsai, W. Nie, C. C.

Stoumpos, M. G. Kanatzidis, S. Tretiak, A. D. Mohite, J. Even, M. Kepenekian, C. Katan, *ACS Nano* **2018**, *12*, 3321.

[26] M. Egginger, S. Bauer, R. Schwödiauer, H. Neugebauer, N. S. Sariciftci, *Monatshefte fur Chemie* **2009**, *140*, 735.

[27] A. R. Stokes, A. J. C. Wilson, *Math. Proc. Cambridge Philos. Soc.* **1942**, *38*, 313.

[28] K. M. Boopathi, R. Mohan, T.-Y. Huang, W. Budiawan, M.-Y. Lin, C.-H. Lee, K.-C. Ho, C.-W. Chu, *J. Mater. Chem. A* **2016**, *4*, 1591.

[29] B. A. Jones, A. Facchetti, M. R. Wasielewski, T. J. Marks, *Adv. Funct. Mater.* **2008**, *18*, 1329.

[30] Y. Yuan, G. Giri, A. L. Ayzner, A. P. Zoombelt, S. C. B. Mannsfeld, J. Chen, D. Nordlund, M. F. Toney, J. Huang, Z. Bao, *Nat. Commun.* **2014**, *5*, 3005.

[31] R. L. Milot, R. J. Sutton, G. E. Eperon, A. A. Haghighirad, J. Martinez Hardigree, L. Miranda, H. J. Snaith, M. B. Johnston, L. M. Herz, *Nano Lett.* **2016**, *16*, 7001.

[32] D. Ma, Y. Fu, L. Dang, J. Zhai, I. A. Guzei, S. Jin, *Nano Res.* **2017**, *10*, 2117.

[33] K. Shibuya, M. Koshimizu, F. Nishikido, H. Saito, S. Kishimoto, IUCr, *Acta Crystallogr. Sect. E Struct. Reports Online* **2009**, *65*, m1323.

[34] V. Georgiou, D. Veksler, J. P. Campbell, P. R. Shrestha, J. T. Ryan, D. E. Ioannou, K. P. Cheung, *Adv. Funct. Mater.* **2018**, *28*, 1705250.

[35] B. Hwang, J.-S. Lee, *Adv. Electron. Mater.* **2019**, *5*, 1800519.

[36] S. P. Senanayak, B. Yang, T. H. Thomas, N. Giesbrecht, W. Huang, E. Gann, B. Nair, K. Goedel, S. Guha, X. Moya, C. R. McNeill, P. Docampo, A. Sadhanala, R. H. Friend, H. Sirringhaus, *Sci. Adv.* **2017**, *3*, e1601935.

[37] M. H. Futscher, J. M. Lee, L. McGovern, L. A. Muscarella, T. Wang, M. I. Haider, A. Fakharuddin, L. Schmidt-Mende, B. Ehrler, *Mater. Horizons* **2019**, *6*, 1497.

[38] M. Abbas, A. Pivrikas, E. Arici, N. Tekin, M. Ullah, H. Sitter, N. S. Sariciftci, *J. Phys. D Appl. Phys* **2013**, *46*, 495105.

[39] Y. J. Lin, Y. C. Lin, *AIP Adv.* **2014**, *4*, 107105.

[40] S. M. Sze, K. K. Ng, in *Phys. Semicond. Devices*, John Wiley & Sons, Inc., Hoboken, NJ, USA, **2006**, pp. 415–465.

[41] C. Joachim, M. A. Ratner, *Proc. Natl. Acad. Sci. U. S. A.* **2005**, *102*, 8801.

[42] H. C. Seong, B. S. Kim, C. D. Frisbie, *Science (80-.).* **2008**, *320*, 1482.

[43] Y. Lin, Y. Bai, Y. Fang, Q. Wang, Y. Deng, J. Huang, *ACS Energy Lett.* **2017**, *2*, 1571.

[44] A. V. Krukau, O. A. Vydrov, A. F. Izmaylov, G. E. Scuseria, *J. Chem. Phys.* **2006**, *125*, 224106.

[45] X. Yang, Z. Chu, J. Meng, Z. Yin, X. Zhang, J. Deng, J. You, *J. Phys. Chem. Lett.* **2019**, *10*, 2892.

[46] A. F. Paterson, Y. H. Lin, A. D. Mottram, Z. Fei, M. R. Niazi, A. R. Kirmani, A. Amassian, O. Solomeshch, N. Tessler, M. Heeney, T. D. Anthopoulos, *Adv. Electron. Mater.* **2018**, *4*, 1700464.

[47] M. Lenzlinger, E. H. Snow, *J. Appl. Phys.* **1969**, *40*, 278.

[48] Y. Wang, Y. Yang, P. Ding, Q. Wei, X. Gao, S. Wang, C. Liu, A. Li, J. Yin, Y. Xia, Z. Liu, *Adv. Electron. Mater.* **2019**, *5*, 1.

[49] S. J. Kim, J. S. Lee, *Nano Lett.* **2010**, *10*, 2884.

[50] Y. H. Chou, S. Takasugi, R. Goseki, T. Ishizone, W. C. Chen, *Polym. Chem.* **2014**, *5*, 1063.

[51] W. Li, F. Guo, H. Ling, P. Zhang, M. Yi, L. Wang, D. Wu, L. Xie, W. Huang, *Adv. Sci.* **2017**, *4*, 1700007.

[52] H. C. Chang, C. L. Liu, W. C. Chen, *Adv. Funct. Mater.* **2013**, *23*, 4960.

[53] Y. Park, K. J. Baeg, C. Kim, *ACS Appl. Mater. Interfaces* **2019**, *11*, 8327.

[54] K. J. Baeg, Y. Y. Noh, H. Sirringhaus, D. Y. Kim, *Adv. Funct. Mater.* **2010**, *20*, 224.

[55] Z. H. Wu, W. J. Sun, H. H. Tian, Z. F. Yu, R. X. Guo, X. Shao, H. L. Zhang, *Adv. Electron. Mater.* **2019**, *5*, 1800598.

[56]   L. A. Frolova, A. A. Rezvanova, V. Z. Shirinian, A. G. Lvov, A. V. Kulikov, M. M. Krayushkin, P. A. Troshin, *Adv. Electron. Mater.* **2016**, *2*, 1500219.

[57]   L. Song, Y. Wang, Q. Gao, Y. Guo, Q. Wang, J. Qian, S. Jiang, B. Wu, X. Wang, Y. Shi, Y. Zheng, Y. Li, *ACS Appl. Mater. Interfaces* **2017**, *9*, 18127.

[58]   K. Z. Du, Q. Tu, X. Zhang, Q. Han, J. Liu, S. Zauscher, D. B. Mitzi, *Inorg. Chem.* **2017**, *56*, 9291.

Figures
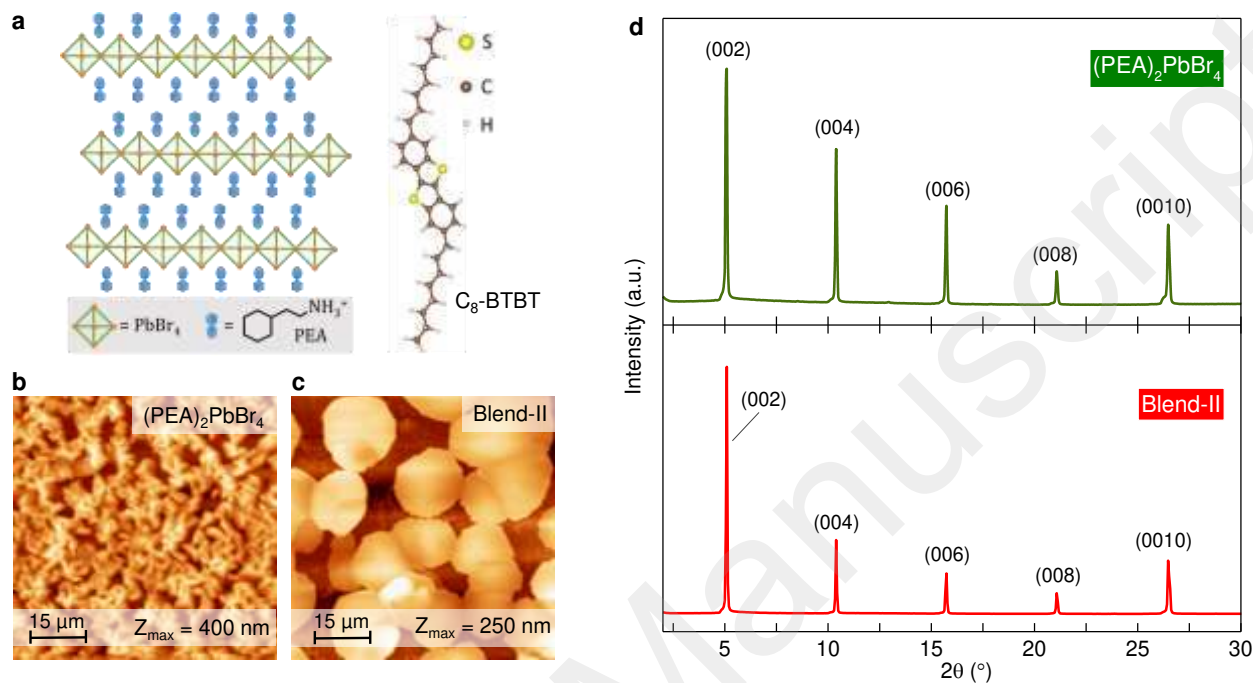
Figure 1. (a) Illustration of the 2D layered perovskite (PEA)$_2$PbBr$_4$ and organic small-molecule C$_8$-BTBT. Atomic force microscopy images of pristine (PEA)$_2$PbBr$_4$ (b), and Blend-II (c) layers. (d) Out-of-plane XRD patterns measured for (PEA)$_2$PbBr$_4$ and Blend-II films.
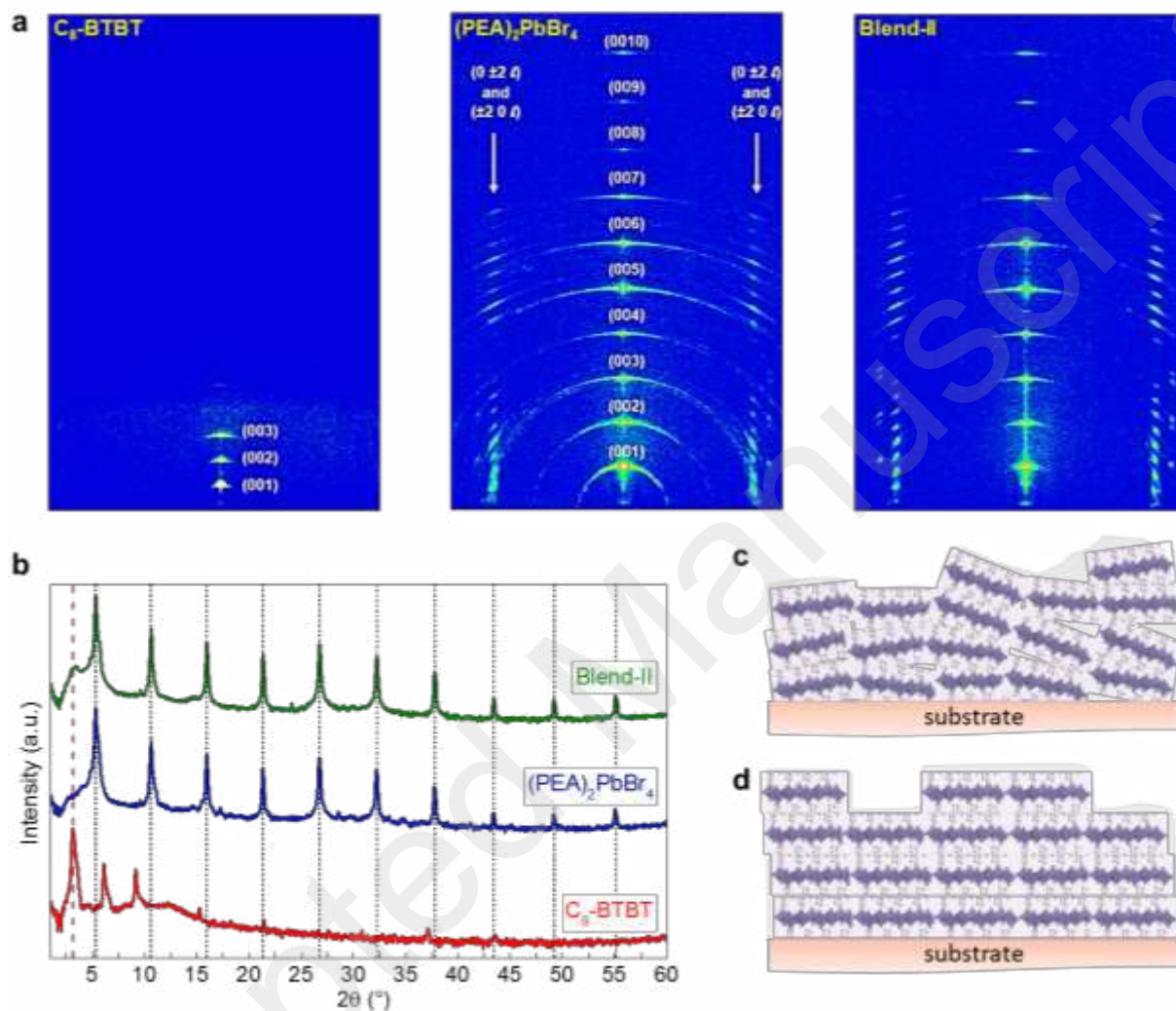
Figure 2. 2D-XRD diffraction pattern of coupled $\theta/2\theta$ scans measured for (a) spin-coated C_8-BTBT, pristine $(PEA)_2PbBr_4$, and Blend-II. (b) 1D diffraction pattern (central slice) with a logarithmic intensity scale. Schematic depiction of the orientation of the 2D-perovskite domains for pristine $(PEA)_2PbBr_4$ (c), and Blend-II (d) layers. In (d) the C_8-BTBT is not shown for simplicity.
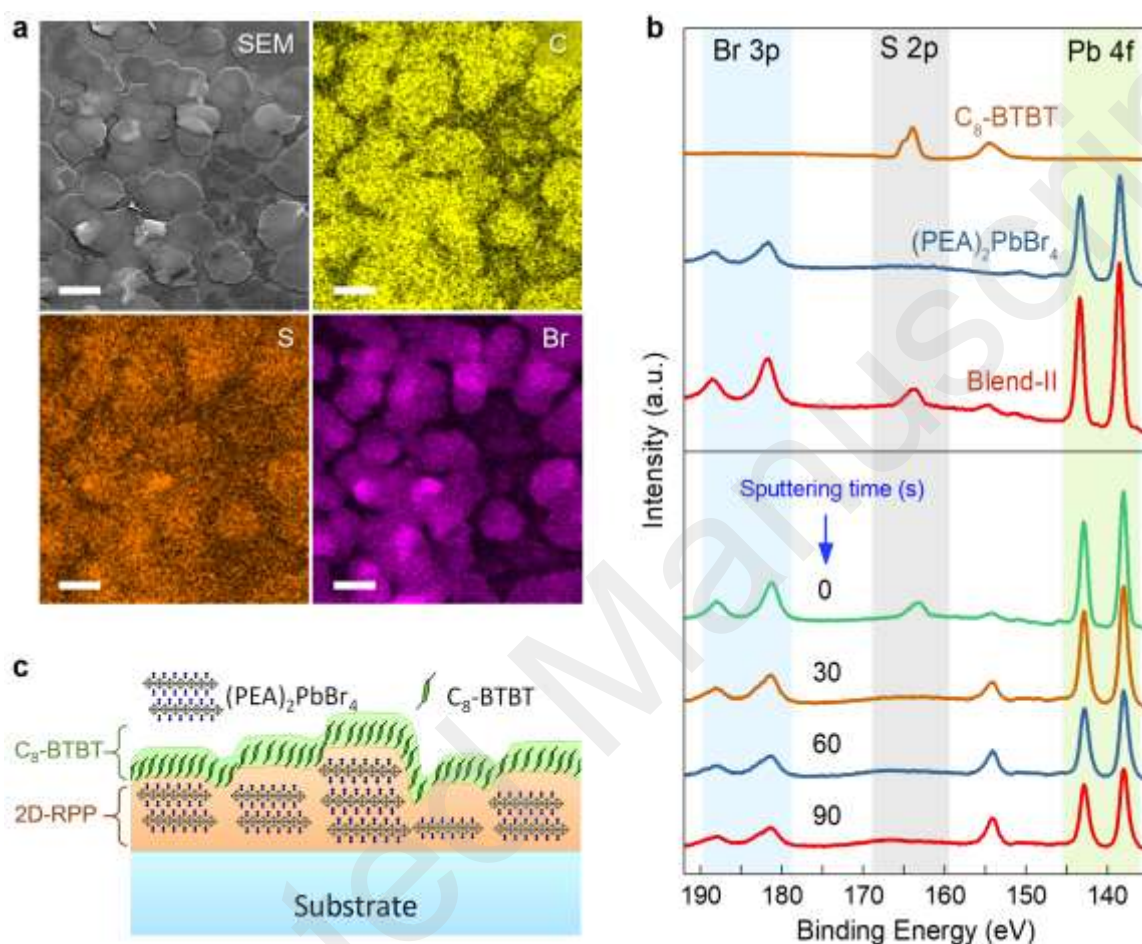
Figure 3. a) SEM-EDS elemental mapping of Carbon (C), Sulfur (S), Bromine (Br) and Led (Pb). In all images, the scale bar is 20 µm. b) XPS spectra in the 195-134 eV range covering the Br 3p, S 2p, Si 2s, and Pb 4f core level peaks in C_8-BTBT, $(PEA)_2PbBr_4$ and Blend-II (top frame) and depth profiling of Blend-II at different sputtering times (bottom frame). c) Schematic illustration of the vertically phase-separated Blend-II layer.
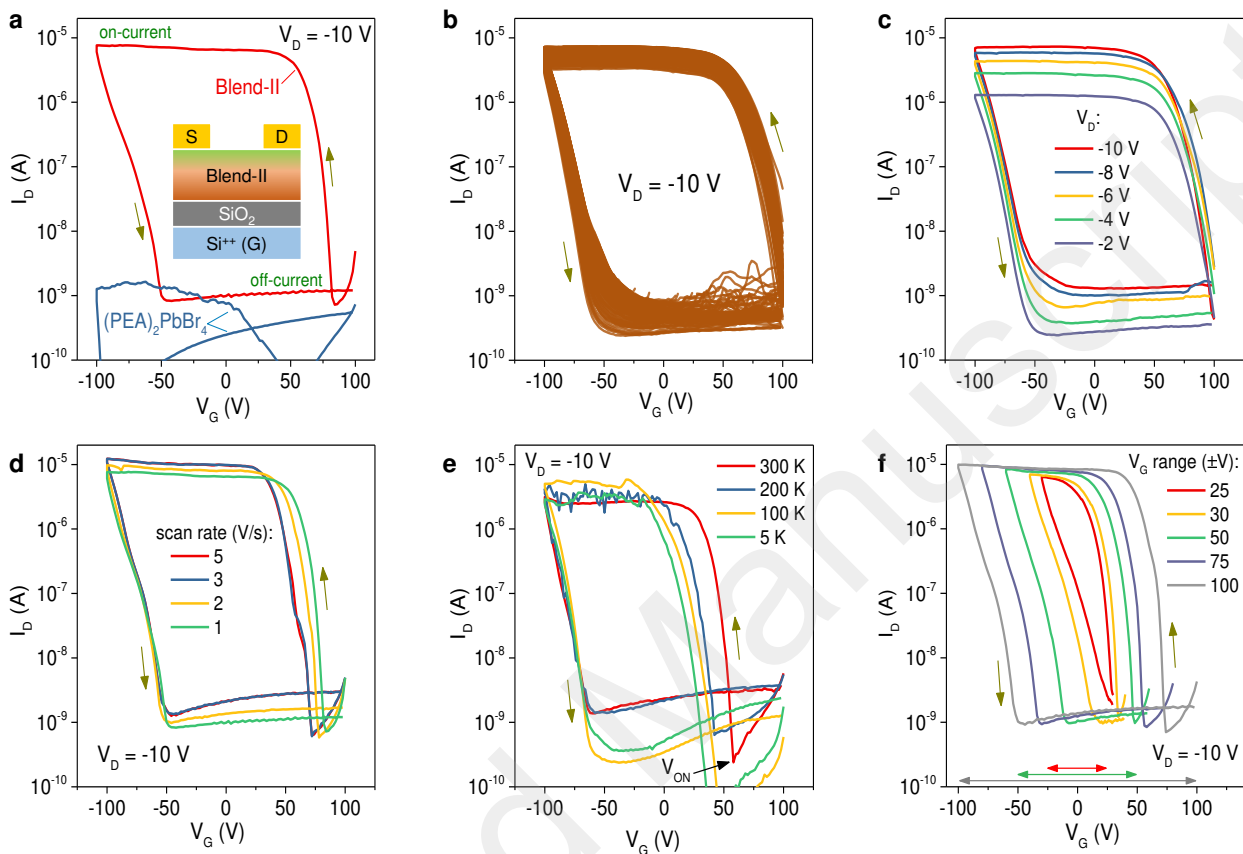
Figure 4. a) Charge transfer characteristics of (PEA)$_2$PbBr$_4$ and Blend-II based FETs. Inset is the schematic of the device. b) Multiple hysteresis loops up to 100 continuous cycles. Device hysteresis behavior with c) drain voltage and d) scan rate. e) Temperature-dependent hysteresis behavior of the memristor. f) Variation in hysteresis window for different gate voltage scan ranges.
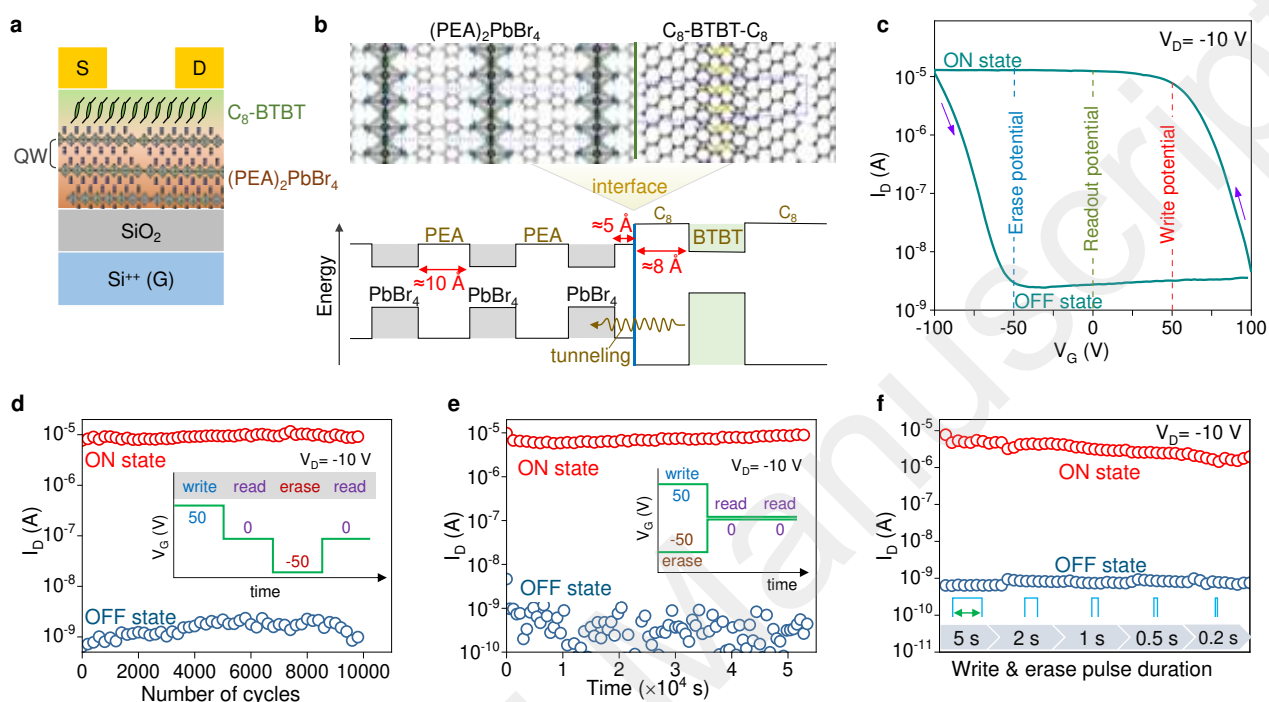
Figure 5. a) Schematic of a transistor incorporating the phase-separated Blend-II as the channel layer. b) Schematic of the energy level alignment between the organic and inorganic counterparts of $(PEA)_2PbBr_4$ and C_8-BTBT. c) Representative transistor transfer curve depicting the programming/reading/erasing potentials used for device testing. d) Endurance performance of the memristor subjected to 10,000 continuous ON-OFF programming cycles. e) Memory retention characteristics monitored for 55,000 s. f) Memory switching behavior using different write/erase pulse width ranging from 5 to 0.2 s.

ToC Text

Blending the organic semiconductor C_8-BTBT with the layered Ruddlesden-Popper phase perovskite $(PEA)_2PbBr_4$ in solution phase facilitates the formation of large and near-single-crystalline quality platelet-like perovskite domains overlaid by a thin layer of the organic molecule. Transistors utilising the $(PEA)_2PbBr_4$/C_8-BTBT bilayer as the channel exhibit unexpectedly large hysteresis and their use as non-volatile memory element is demonstrated.

Murali Gedda, Emre Yengel, Hendrik Faber, Fabian Paulus, Joshua A. Kreß, Ming-Chun Tang, Siyuan Zhang, Christina A. Hacker, Prashant Kumar, Dipti R. Naphade, Yana Vaynzof, George Volonakis, Feliciano Giustino, and *Thomas D. Anthopoulos*
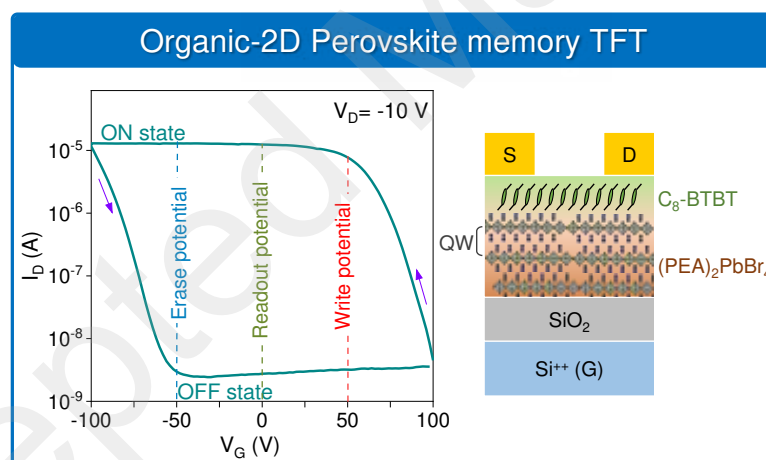
Supporting Information

Ruddlesden-Popper Phase Hybrid Halide Perovskite/ Small-Molecule Organic Blend Memory Transistor

Murali Gedda*, Emre Yengel, Hendrik Faber, Fabian Paulus, Joshua A. Kreß, Ming-Chun Tang, Siyuan Zhang, Christina A. Hacker, Prashant Kumar, Dipti R. Naphade, Yana Vaynzof, George Volonakis, Feliciano Giustino, and Thomas D. Anthopoulos*
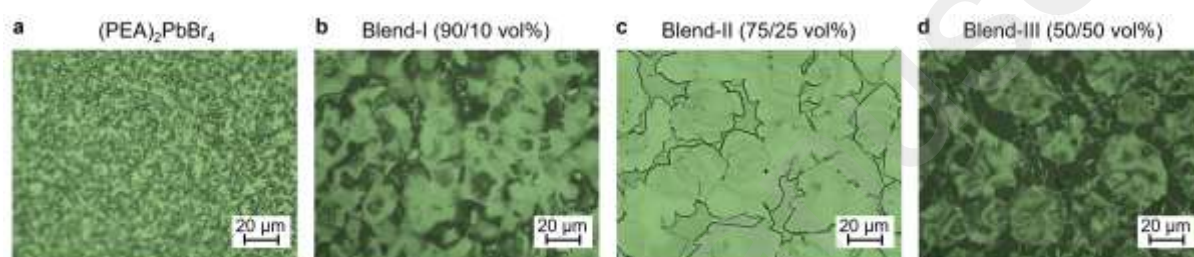
Figure S1. Optical micrographs of a) $(PEA)_2PbBr_4$, b) Blend-I, c) Blend-II and d) Blend-III perovskite films.
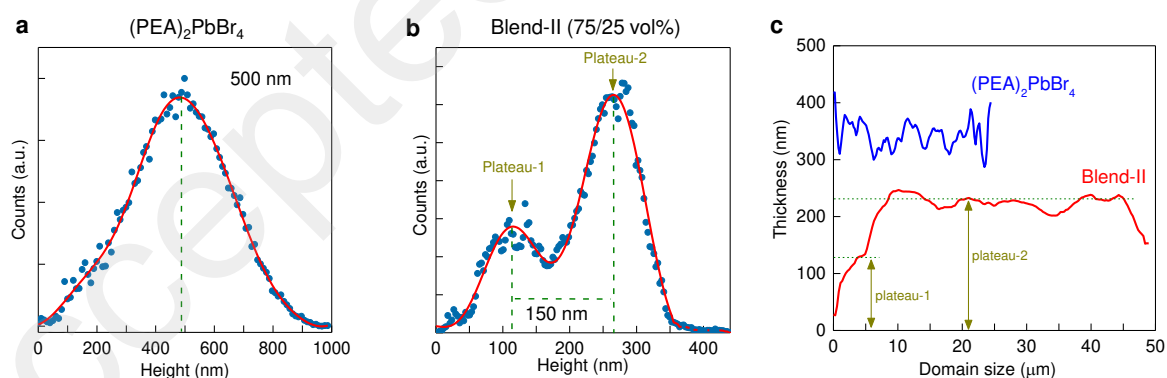

Figure S2. Height histograms extracted from AFM topographic images shown in **Figure 1** for the neat $(PEA)_2PbBr_4$ (a), and Blend-II (b), layers. (c) Radial average profiles extracted from the same AFM images for the neat $(PEA)_2PbBr_4$ and Blend-II layers.
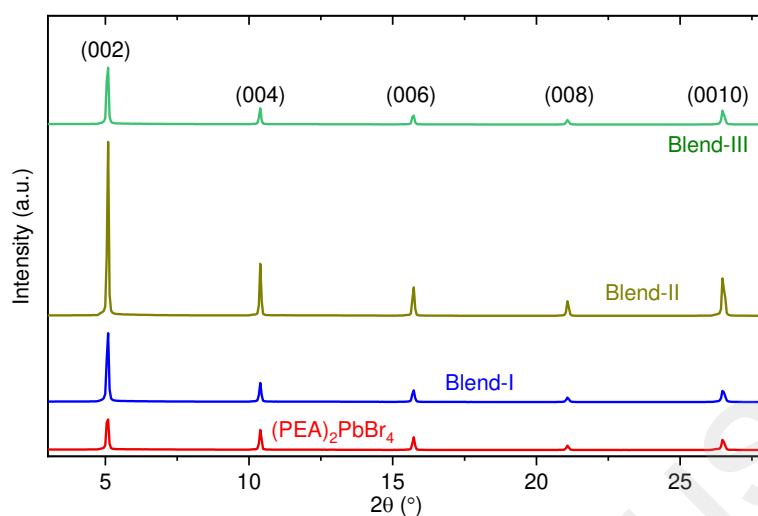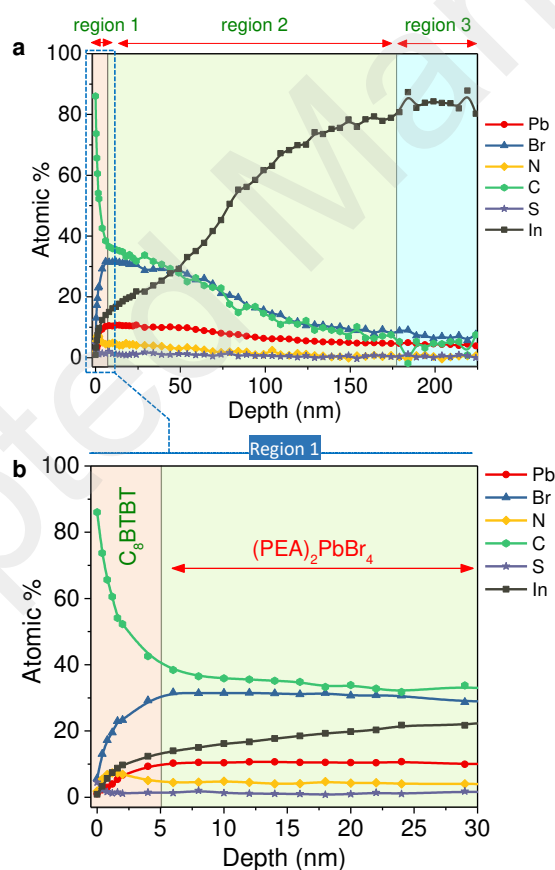
Figure S3. XRD patterns measured for neat and all three blend perovskite films.
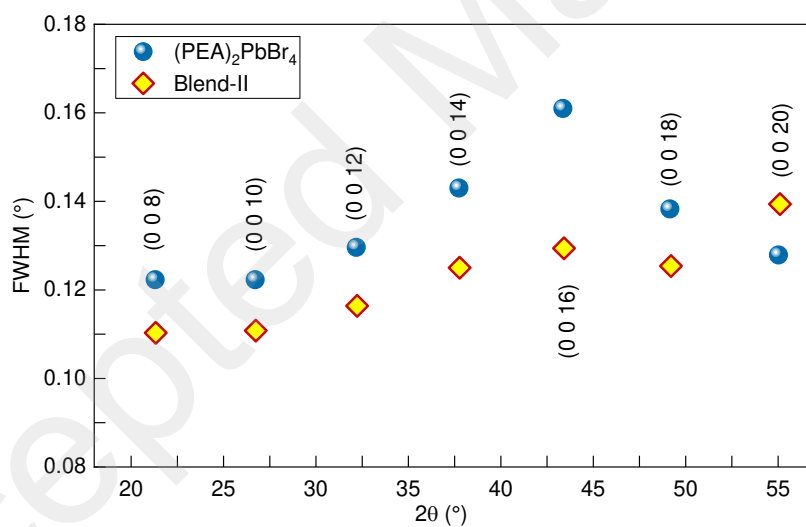

Figure S4. Comparison of the FWHM for higher-order (0 0 *l*) reflections after fitting Pseudo

Voigt functions. The Blend always exhibits sharper reflections indicating the presence of larger

crystallites.
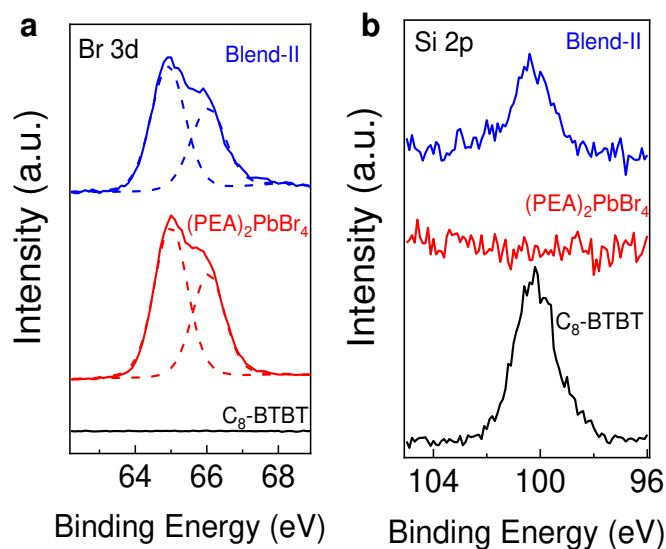
Figure S5. XPS spectra for Br 3d and Si 2p in C_8-BTBT, $(PEA)_2PbBr_4$, and Blend-II films.

Figure S6. (a) Elemental profiles extracted from X-ray photoemission spectroscopy depth profiling measurements on C_8-BTBT:$(PEA)_2PbBr_4$ on ITO. (b) Magnified view of region 1 and 2 shown in (a).
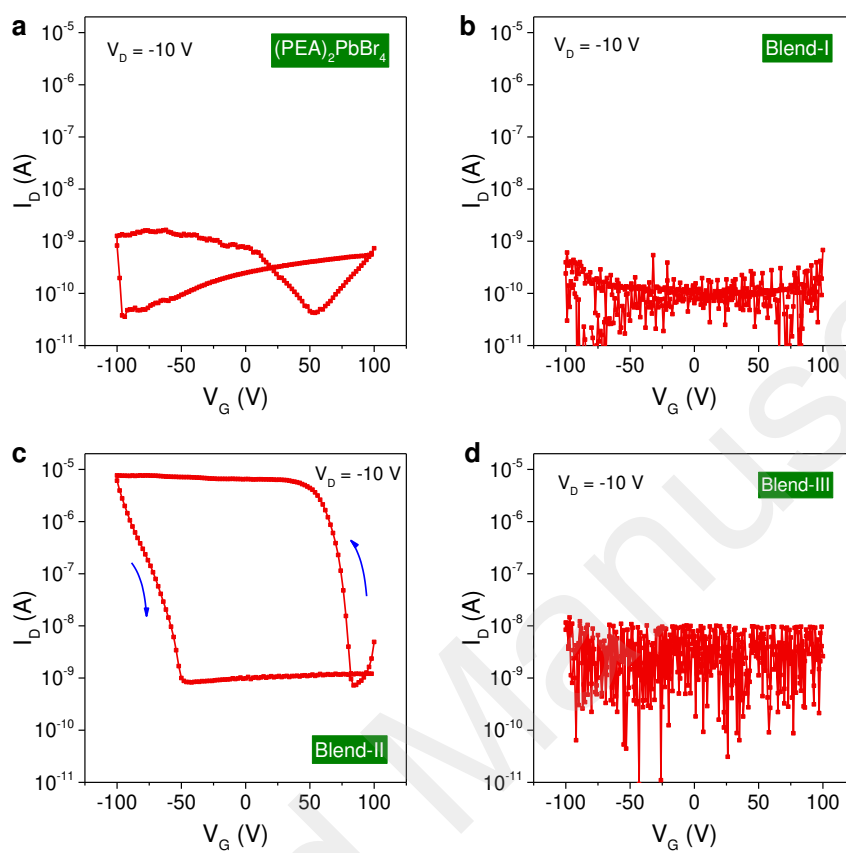
Figure S7. Transfer characteristics at fixed drain bias -10 V of a) $(PEA)_2PbBr_4$, b) Blend-I, c) Blend-II and d) Blend-III perovskites based FETs.
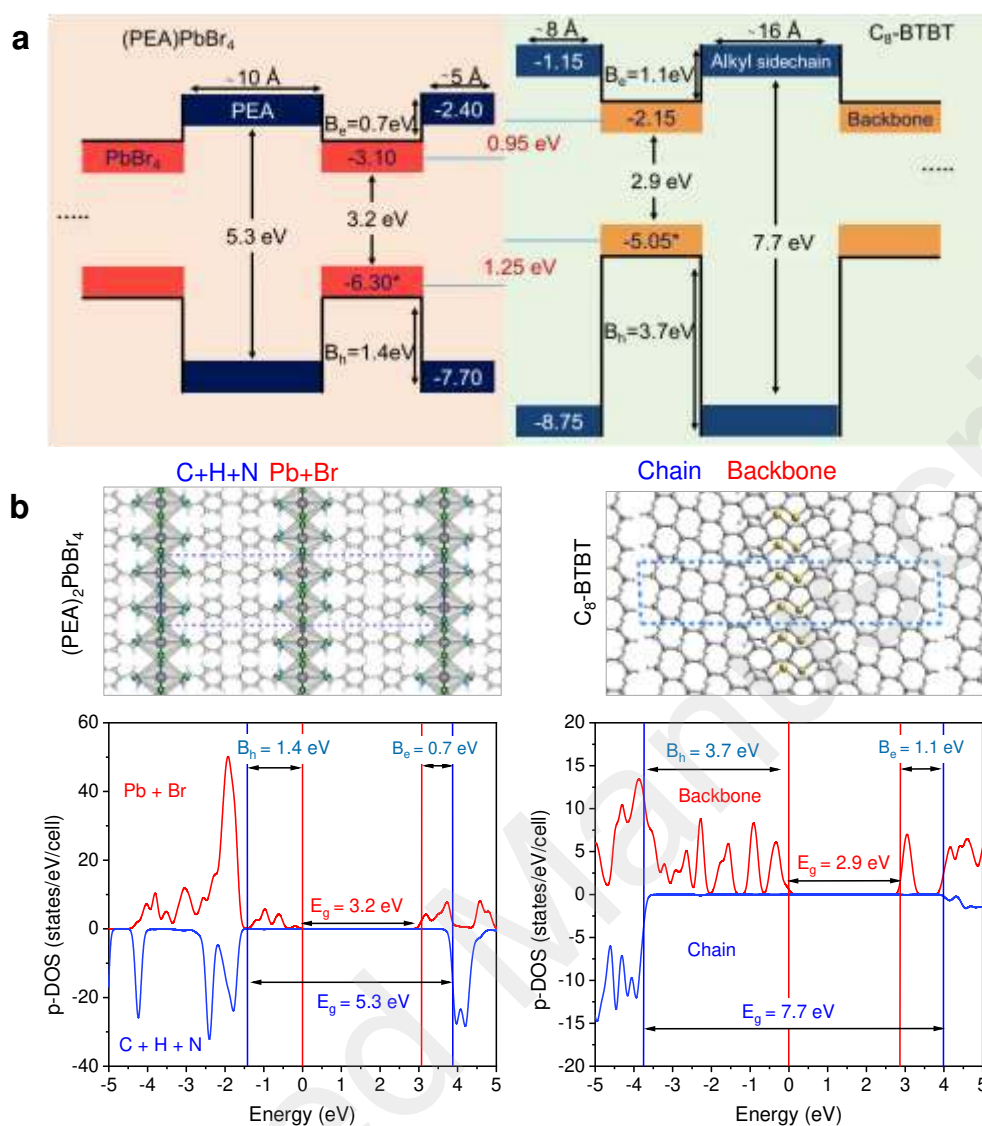
Figure S8. Energy level alignment between C_8-BTBT and $(PEA)_2PbBr_4$ (a), constructed using the atomistic model and projected density-of-states within DFT-HSE hybrid functional for the inorganic (red) and organic (blue) part of $(PEA)_2PbBr_4$ and C_8-BTBT (b). The blue dashed line on the atomistic models of $(PEA)_2PbBr_4$ and C_8-BTBT shows the lattice unit-cell.
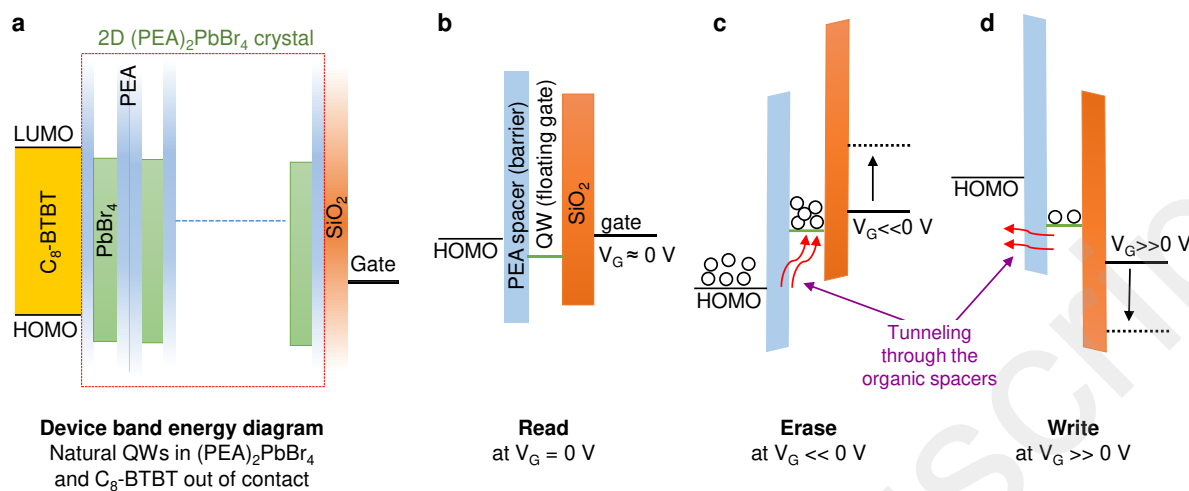
Figure S9. (a) Simplified energy band diagram of the Blend-II based floating gate transistor. Energy band diagrams of the same device under different operational modes: (b) read, (c) write, and (d) erase bias conditions. Open circles represent hole charge carriers.
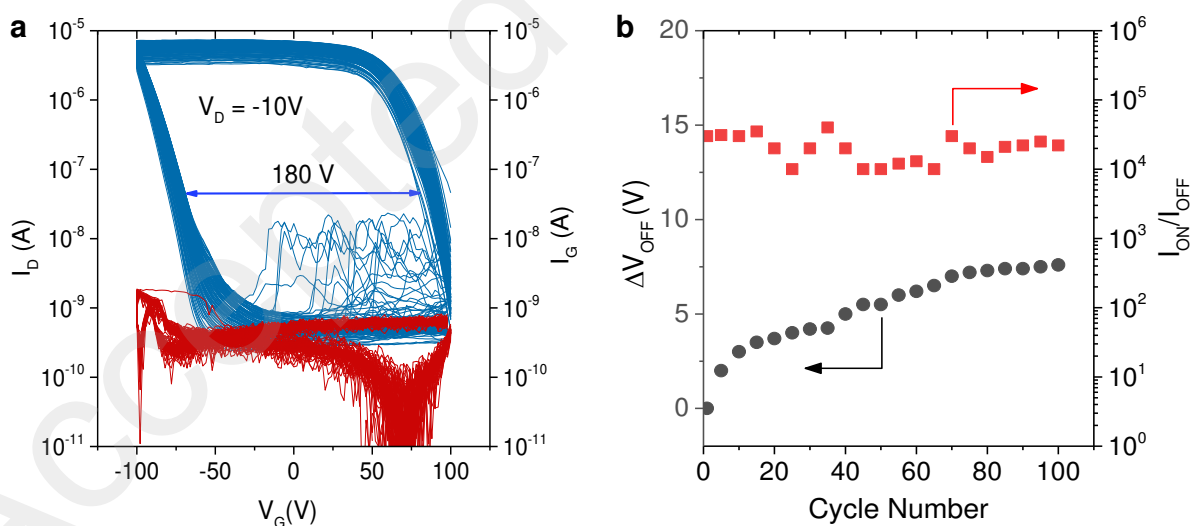
Figure S10. (a) 100 consecutively measured transfer characteristics obtained for a Blend-II memory transistor. (b) Change in switch-off voltage (ΔV_{OFF}) and ON/OFF ratios as a function of measurement cycle. The field-effect hole mobility extracted from the forward sweep in (a) was approximately 6×10^{-2} cm^2 V^{-1}s^{-1}.

Theoretical calculation

Calculations have been performed using the experimental structure of $(PEA)_2PbBr_4$, which is deposited in the Cambridge Structure Database (1542460) and Ref. Du *et al.*[58] The lattice is orthorhombic with lattice parameters of a = 33.35 Å, b = 8.146 Å, c = 8.123 Å. The atomistic model is shown in **Figure S8**. The structure is a two-dimensional halide perovskite, with n=1, and the spacer is the organic PEA (NH_2-CH_2-Ph). The unit cell has two layers of $PbBr_4$ octahedra, which results in a total of 164 atoms. We perform calculations without optimizing the structure (fixed atoms + cell) employing the HSE hybrid functional. We calculate the projected density-of-states (p-DOS) that is shown in **Figure S8b**. Blues are the contributions of the organic part (C, N, H atoms) and red shows the inorganic part (Pb+Br). The bandgap (E_g) of the compound is found at 3.2 eV, and the valence band top and bottom are comprised of Pb and Br, as expected. The first occupied states that belong to the organic parts are found at 1.4 eV below the valence band top, and the first unoccupied states at 0.7 eV above the conduction bands. The total bandgap for the organic part of perovskite obtained as 5.3 eV. **Figure S8a** shows the final confinement picture. The size of the confinement is 10.7 Å for the wide-bandgap organic part, and 6 Å for the semiconducting inorganic sites. This level diagram corresponds to a type-I band alignment. Similar calculations are extended to the organic small molecule, C_8-BTBT using the experimental structure from a reference.[46] The bandgap (E_g) of the small molecule is found at 2.9 eV. The first occupied states that belong to the 1-octyl part of C_8-BTBT are found at 3.7 eV below the valence band top, and the first unoccupied states at 1.1 eV above the conduction bands. The total bandgap for the 1-octyl side chain of small molecule estimated as 7.7 eV.

Table S1. Calculated crystallite sizes of $(PEA)_2PbBr_4$ and Blend-II films using the Debye-Scherer equation.

Material	2θ (°)	FWHM (2θ)	Crystallite size (nm)
$(PEA)_2PbBr_4$	5.28	0.1113	74
Blend -II	5.28	0.0676	123

Table S2. Comparison of key operating parameters of Blend-II based transistors with organic-based TFT memory devices from the literature.

Channel material	Dielectric material	Charge storage element	Operating voltage (V_{OP})	Memory window ΔV_M (V)	$\dfrac{\Delta V_M}{V_{OP}}$	Endurance cycles	Writing/ erasing speed	Ref.
Pentacene	Al_2O_3	ZnTe	±15	10	0.33	---	---	[48]
Pentacene	PVP	Au NP	±90	10	0.05	700	1 s	[49]
BPE-PTCDI	SiO_2/300 nm	PVTT	±100	81	0.40	100	>10 s	[50]
Pentacene	SiO_2/300 nm	P13	±120	60	0.25	3000	1 s	[51]
P3HT	Al_2O_3	Au-NH_2	±15	10.6	0.35	100	1 s	[52]
N(PTPMA)$_3$:TIPS-PEN	SiO_2/300 nm	PS Brush	-120 to 100	55	0.25	100	1 s	[53]
F8T2	PS	Au NPs	±90	30	0.16	---	1 s	[54]
IPPA-Cl	PS	Doped PS	±30	40.8	0.68	100	10 s	[55]
C_{60}	Al_2O_3	Photo chrome	3 to -10	10	0.76	100	10-30 ms	[56]
C_8-BTBT	PMMA	P(VDF-TrFE)	±15	12	0.40	100	4 ms	[57]
C_8-BTBT	SiO_2/300 nm	$(PEA)_2PbBr_4$	±100	180	0.9	>10000	0.2 s	This work